

Short Gamma-Ray Bursts from Binary Neutron Star Mergers

Roland Oechslin and Thomas Janka

Max Planck-Institut für Astrophysik, Karl Schwarzschild-Str. 1, 85741 Garching, Germany

Abstract. We present the results from new relativistic hydrodynamic simulations of binary neutron star mergers using realistic non-zero temperature equations of state. We vary several unknown parameters in the system such as the neutron star (NS) masses, their spins and the nuclear equation of state. The results are then investigated with special focus on the post-merger torus-remnant system. Observational implications on the Gamma-ray burst (GRB) energetics are discussed and compared with recent observations.

Keywords: Gamma-Ray bursts, Hydrodynamics, Relativity and gravitation, Neutron stars

PACS: 98.70.Lt, 95.30.Lz, 95.30.Sf, 97.60.Jd

INTRODUCTION

Merger events of binary neutron stars (BNS) and neutron star - black hole (NS+BH) binaries do not only belong to the strongest known sources of gravitational wave (GW) radiation, they are also widely favored as origin of the subclass of short, hard Gamma-ray bursts (GRBs) [1, 2, 3, 4, 5]. The recent first good localizations of short bursts by the *Swift* and *HETE* satellites were interpreted as a possible confirmation of this hypothesis [6, 7, 8, 9, 10], because the bursts have observational characteristics which are different from those of long GRBs, but which are in agreement with expectations from compact object mergers as e.g. the energetics and the association with old stellar populations. The central engines of such bursts are still poorly understood and observationally undetermined. But it seems unlikely that the energies required for typical short GRBs are set free during the dynamical phase of the merging of two NSs. Instead, the following secular accretion phase in a postmerger system consisting of a central BH and a surrounding torus seems to be a much more promising source (see e.g., [11, 12, 13, 14, 15]) provided the torus is sufficiently massive. Thermal energy release preferentially above the poles of the BH by the annihilation of neutrino-antineutrino ($\nu\bar{\nu}$) pairs can lead to collimated, highly relativistic jets of baryonic matter [16]. The gamma radiation is then produced in internal shocks when different blobs of ultrarelativistic matter in the jet collide with each other. When the jet hits the ambient interstellar medium, the less energetic afterglow radiation is produced.

Torus mass as well as BH mass and rotation are thus crucial parameters that determine the energy release from the merger event. Here, we summarize results from our recent 3D relativistic hydrodynamics simulations of BNS mergers [17, 18] to investigate the dependence of the torus and BH properties on the initial BNS parameters like the nuclear EoS, the NS masses and mass ratio and the NS spins.

In the following, we define the torus by the condition that the specific angular momentum of a fluid element in the torus has to be larger than the innermost stable circular orbit of a Kerr black hole with the mass and the rotation parameter of the remnant. The latter in turn is defined as all the matter which is not in the torus.

RESULTS FROM RELATIVISTIC HYDRODYNAMICS SIMULATIONS OF BNS MERGERS

Using our relativistic smooth particle hydrodynamics (SPH) code [18], we have simulated a large set of BNS merger models, varying the EoS, the initial neutron star mass ratio, the total mass and the NS spins.

We have used two realistic, non-zero temperature EoSs whose supranuclear parts base upon two fundamentally different approaches to determine the nuclear interaction. The EoS of Shen et al. [19, 20] (“Shen-EoS”) bases on the phenomenological relativistic mean field (RMF) approach, while the EoS of Lattimer and Swesty [21] (“LS-EoS”) employs the finite-temperature compressible liquid droplet model for the nucleus [22]. In addition, we consider an ideal gas EoS whose adiabatic index Γ is adjusted to fit the Shen-EoS in the supranuclear regime.

TABLE 1. Setup parameters and characteristic data of our considered models. M_1 and M_2 denote the individual gravitational masses in isolation while $M_{\text{sum}} = M_1 + M_2$ stands for the sum of the two (Note that the total gravitational mass M is slightly smaller than M_{sum} because M also involves the negative gravitational binding energy between the two stars.). M_0 is the total baryonic mass, whereas $q = M_1/M_2$ and $q_M = M_{0,1}/M_{0,2}$ is the gravitational and baryonic mass ratio, respectively. ‘Shen’ stands for the full, finite temperature Shen-EoS, ‘Ls’ denotes the Lattimer-Swesty-EoS and ‘ideal gas’ means ideal gas EoS. The NS spin states are denoted as ‘irrot’ for irrotating, ‘corot’ for corotating, ‘counter’ for counterrotating, ‘oppo’ for oppositely oriented spins and ‘tilted’ for a spin orientation tilted relative to the orbital spin. More specifically, we choose in model S1414t1 $\Omega_1 = 0$ and $\Omega_2 = 0.041 * (0, 1, 0)$ (in cartesian coordinates) which corresponds to a spin period of the second NS of ~ 1 ms, while in model S1414t2, $\Omega_1 = 0.01 * (0, 1, 1)$ and $\Omega_2 = 0.01 * (0, -1, 1)$ is chosen. T_{max} is the maximum temperature in MeV reached in the system during the whole evolution. It is obtained by averaging the particle temperatures on a grid of 1.5km side length. $a_{\text{merging}} = J_{\text{merging}}/M_{\text{merging}}^2$ is the (total) spin parameter measured immediately after merger and M_{torus} denotes the estimated (baryonic) torus mass. Note that in model LS1216 the maximal temperature and the torus mass cannot be determined because the merger remnant collapses immediately after merging.

Model	M_1	M_2	M_{sum}	M_0	q	q_M	EoS	Spin	T_{max}	a_{merging}	M_{torus}
S1414	1.4	1.4	2.8	3.032	1.0	1.0	Shen	irrot × ×	52	0.91	0.06
S138142	1.38	1.42	2.8	3.032	0.97	0.97	Shen	irrot × ×	50	0.90	0.06
S135145	1.35	1.45	2.8	3.034	0.93	0.93	Shen	irrot × ×	50	0.90	0.09
S1315	1.3	1.5	2.8	3.037	0.87	0.86	Shen	irrot × ×	50	0.90	0.15
S1216	1.2	1.6	2.8	3.039	0.75	0.73	Shen	irrot × ×	54	0.89	0.23
S1515	1.5	1.5	3.0	3.274	1.0	1.0	Shen	irrot × ×	67	0.89	0.05
S1416	1.4	1.6	3.0	3.274	0.88	0.86	Shen	irrot × ×	55	0.89	0.17
S1317	1.3	1.7	3.0	3.279	0.76	0.75	Shen	irrot × ×	65	0.88	0.23
S119181	1.19	1.81	3.0	3.289	0.66	0.63	Shen	irrot × ×	57	0.87	0.24
S107193	1.07	1.93	3.0	3.306	0.55	0.52	Shen	irrot × ×	70	0.84	0.26
S1313	1.3	1.3	2.6	2.800	1.0	1.0	Shen	irrot × ×	52	0.93	0.08
S1214	1.2	1.4	2.6	2.799	0.86	0.85	Shen	irrot × ×	43	0.93	0.20
S1115	1.1	1.5	2.6	2.807	0.73	0.71	Shen	irrot × ×	50	0.92	0.23
P1315	1.3	1.5	2.8	3.064	0.87	0.86	ideal gas	irrot × ×		0.90	0.15
LS1414	1.4	1.4	2.8	3.077	1.0	1.0	Ls	irrot × ×	175	0.86	0.03
LS1216	1.2	1.6	2.8	3.087	0.75	0.73	Ls	irrot × ×		0.85	-
S1414co	1.4	1.4	2.8	3.032	1.0	1.0	Shen	corot ↑ ↑	40	0.98	0.24
S1414ct	1.4	1.4	2.8	3.032	1.0	1.0	Shen	counter ↓ ↓	74	0.85	0.04
S1414o	1.4	1.4	2.8	3.032	1.0	1.0	Shen	oppo ↑ ↓	46	0.92	0.11
S1414t1	1.4	1.4	2.8	3.032	1.0	1.0	Shen	tilted ← ×	59	0.95	0.20
S1414t2	1.4	1.4	2.8	3.032	1.0	1.0	Shen	tilted ↗ ↖	39	0.98	0.26
S1216co	1.2	1.6	2.8	3.039	0.75	0.73	Shen	corot ↑ ↑	48	0.98	0.30
S1216ct	1.2	1.6	2.8	3.039	0.75	0.73	Shen	counter ↓ ↓	73	0.84	0.20

Initial data is obtained using a relaxation technique which drives the system into an equilibrium velocity field which is given by the orbital separation, the NS spins Ω_1 and Ω_2 , respectively and the orbital angular velocity Ω . The latter is iteratively determined such that an orbital equilibrium state between gravitational and centrifugal force is established (see [18] for an extensive description). The NS spins are chosen either to be zero (irrotating NSs), or to be equal (corotating NSs) or opposed (counterrotating NSs) to the orbital spin. A few cases with non-aligned NS spins have also been considered (see Tab. 1).

In addition, we assume the initial NSs to be cold and to be in neutrino-less beta-equilibrium which determines the initial distribution of the internal energy u and the electron fraction Y_e (In the ideal gas case, the polytropic relation $u = K\rho^{\Gamma-1}$, with K fitted to the Shen-EoS, is employed to initialize the internal energy). In Tab. 1, we summarize the parameters of our models. The simulations are carried out with typically 400’000 SPH particles from slightly outside the innermost stable circular orbit, through the late inspiral, merging and torus formation until either the collapse of the merger remnant sets in, or a quasi-stationary torus-remnant state has formed.

In models with a mass ratio considerably different from unity, e.g. in models S107193, S1216 or S1317, the less massive but larger star is tidally elongated and disrupted to form a long spiral arm which is largely accreted onto its more massive merger partner. This leads to a non-axisymmetric, differentially rotating central object and a thick massive torus around it. The core of the central remnant forms out of the more massive NS while the accreted material from the less massive partner is wound up to end in the outer shells of the remnant. The material sitting in the spiral arm tip receives enough angular momentum due to a ‘sling-shot-effect’ to escape accretion and to contribute to the

main part of the future torus. This carries a significant amount of the angular momentum from the remnant out into the torus (see Fig. 2). On the other hand, in case of a mass ratio near unity, as eg. in S1414 or S138142 the two partners smoothly plunge together without any disruption and formation of a primary spiral arm. The two original NS cores are kept mostly intact during merging and form together a rotating twin-core, bar-like structure at the center of the merger remnant. This rotating bar drives the formation of secondary spiral arms at the remnant surface after the dynamical merger phase and leads to ejection of material into a small torus. Note that primary spiral arms and large torus masses may still form in these systems, if the initial NS spin setup is favourable, e.g. in case of corotating NSs.

For fixed EoS and NS spin, we find, that the torus mass depends roughly linear on the mass ratio for q -values larger than about 0.8, whereas below that point, the torus mass saturates at about $M_{\text{torus}} \simeq 0.25M_{\odot}$. In total, the torus masses range from about $0.05M_{\odot}$ at $q = 1$ to $0.25M_{\odot}$ at $q = 0.55$ (see Fig. 1, panel (b)).

The NS spin setup mainly determines the total amount of angular momentum in the system and thus directly influences the large-scale postmerger evolution, the amount of material carried into the torus and the spin parameter of the merger remnant. The latter particularly influences the torus mass via our definition of the torus. If the NS are initially corotating, the increase in total angular momentum is about 8% compared to the irrotating case. Similarly, counterrotating NSs decrease the total angular momentum by the same amount.

We find, for fixed EoS (Shen-EoS) and mass ratio ($q = 1$), that the torus mass is indeed mainly determined by the amount of total angular momentum available in the system whereas details in the merger dynamics are of minor importance. Models with a different spin setup, but a similar total angular momentum yield comparable torus masses. This is the case for models S1414co (corotating) and S1414t2 (Tilted spins summing up to a total spin in z-direction), and, to a smaller extent, for models S1414 (no spins) and S1414o (oppositely oriented spins). This suggests that the torus mass dependence on the NS spin setup can be approximately reduced to a single parameter, the total angular momentum in the system (see Fig. 1, panel (a)). In total, we find torus mass values between $0.04M_{\odot}$ for counterrotating NSs and $0.3M_{\odot}$ for corotating NSs.

The EoS influences the merger dynamics and postmerger outcome in different ways. Initially more compact NSs, as obtained with a soft or compressible EoS, lead to a longer inspiral phase because the tidal instability sets in at a smaller orbital separation. Therefore, more angular momentum is carried away by gravitational wave radiation and the angular momentum in the post-merger system is reduced which favours a smaller torus. On the other hand, the angular momentum transport through non-axisymmetric motion, as e.g. a rotating bar-like core, or through numerical viscosity is found to be more efficient if the remnant is more compact and more rapidly rotating. This in turn favours a larger torus. In model LS1414 (see Fig. 1, panel (c)), about twice as much of the angular momentum is radiated away (15% compared to 8% in model S1414) and the torus mass shortly (3ms) after merger is about half as large ($0.03M_{\odot}$ versus $0.06M_{\odot}$). During the following post-merger evolution the torus grows continuously. The ideal gas model P1315 leads almost to the same torus mass as the Shen-EoS model S1315. This suggests that the torus mass is determined by the supranuclear part of the EoS.

IMPLICATIONS FROM OBSERVATIONS OF SHORT GRBS

In this section we discuss the implications to the postmerger system properties from the recent observations and locations of six short GRBs by the Swift and HETE satellites. Several observational results suggest, that at least part of the short GRBs may come from binary NS mergers. Short GRBs seem to be partially associated with elliptical galaxies where star formation has stopped long ago. They also seem not to be associated with supernovae. This is consistent with the long inspiral evolution of binary NS systems prior to merger (see e.g. [23]).

From the measured isotropic equivalent energy $E_{\gamma,iso}$, we can now estimate, within the merger model, the mass which is accreted onto the central BH:

$$E_{\gamma,iso} = f_1 f_2 f_3 f_4 f_{\Omega}^{-1} M_{\text{accreted}}$$

Here, f_1 is the efficiency at which the accreted rest mass energy is converted to neutrino emission, f_2 is the conversion efficiency of neutrino-antineutrino annihilation to e^{\pm} pairs, f_3 is the fraction of the e^{\pm} -photon fireball energy which drives the ultrarelativistic outflow with Lorentz factors $\Gamma > 100$ as required by GRBs, f_4 is the fraction of the energy in ultrarelativistic jet matter which can be converted to gamma radiation in dissipative processes that occur in internal shocks in the jet and $f_{\Omega} = 2\Omega_{\text{jet}}/(4\pi) = 1 - \cos\theta_{\text{jet}}$ denotes the jet collimation factor defined as the fraction of the sky covered by the two polar jets (with semi-opening angles θ_{jet} and solid angles Ω_{jet}).

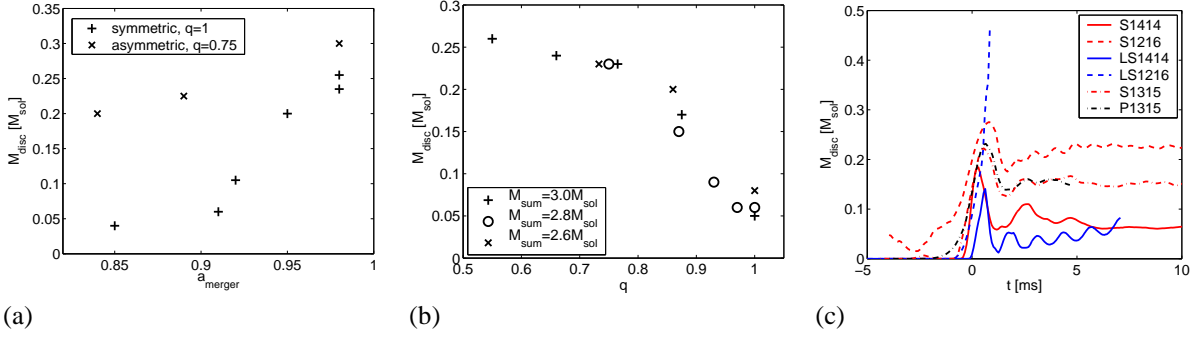


FIGURE 1. (a) Torus masses versus total spin parameter $a_{\text{merger}} = J_{\text{merger}}/M_{\text{merger}}^2$ of the system shortly after merger. Plotted are two series of models, with fixed EoS and with mass ratio $q=1$ ('+'-signs) and $q=0.75$ ('x'-signs), respectively. (b) Torus masses versus mass ratio q . Three different values of the total gravitational mass are chosen and marked with '+'-signs ($M_{\text{sum}} = 3.0 M_{\odot}$), circles ($M_{\text{sum}} = 2.8 M_{\odot}$) and 'x'-signs ($M_{\text{sum}} = 2.6 M_{\odot}$). These models use the Shen-EoS and are initially irrotating. (c) Torus masses for different EoSs. The Shen-EoS models are plotted in red, while the LS-EoS models are colored in blue and the ideal gas EoS model in black. The more compact LS-EoS model LS1414 leads to a significantly smaller torus mass than the corresponding Shen-EoS model S1414 shortly after merger. During the subsequent evolution, angular momentum transport by non-axisymmetric tidal interaction and numerical viscosity increases the torus mass. Note that the peaks initially after merger are an artifact of the non-linear feedback between torus mass, remnant mass and the angular momentum of the last stable orbit in our torus-determination algorithm.

TABLE 2. Estimated accreted masses, M_{acc} , and lower bounds for the average mass accretion rates. The quantity $E_{\gamma,\text{iso}}$ is the isotropic-equivalent γ -ray burst energy (corrected for the cosmological redshift z of the burst), and t_{γ} is the GRB duration at the source, computed as $t_{\gamma} = T_{90}/(1+z)$ from the measured 90%-inclusive interval of high-energy emission. The observational data were taken from Fox et al. [6] and Soderberg et al. [36].

GRB	z	t_{γ}	$E_{\gamma,\text{iso}}$	M_{acc}	\dot{M}_{acc}
Unit		sec.	ergs	M_{\odot}	$M_{\odot}/\text{sec.}$
050509b	0.225	0.033	4.5×10^{48}	2.5×10^{-3}	0.08
050709	0.160	0.060	6.9×10^{49}	3.8×10^{-2}	0.6
050724	0.258	2.4	4.0×10^{50}	2.2×10^{-1}	0.09
050813	0.722	0.35	6.5×10^{50}	3.6×10^{-1}	1.0
051221	0.5459	0.16	2.4×10^{51}	1.3	8.13

“Typical” values from merger and accretion simulations are: $f_1 \sim 0.05$ [15, 24], $f_2 \sim 0.001 \dots 0.01$ [12, 24], $f_3 \sim 0.1$, $f_{\Omega} \sim 0.01 \dots 0.05$ [16] and $f_4 \lesssim 0.2$ [25, 26, 27, and references therein]. To estimate the accreted mass, we use the set

$$(f_1, f_2, f_3, f_{\Omega}, f_4) = (0.1, 0.01, 0.1, 0.01, 0.1) \quad (1)$$

to obtain the values in Tab. 2. In addition, we can calculate the average accretion rate $\dot{M}_{\text{acc}} = M_{\text{acc}}/t_{\text{acc}} \gtrsim M_{\text{acc}}/t_{\gamma}$ assuming that the observed GRB duration t_{γ} is an upper limit to the accretion time t_{acc} [16]. Despite of the crude assumption in (1), we find in nearly all cases values for the torus mass in the range obtained from our theoretical models. In addition, the estimated mass accretion rates lie in the ballpark of the results from postmerger accretion disk simulations [12, 28, 24, 15]. Note however that all the f-factors have large uncertainties and are likely not to be constant but to depend on the torus mass. For example, the neutrino annihilation efficiencies sensitively depend on the temperature which in turn depends on the fluid density and thus on the torus mass. Therefore, the large values for the torus mass and the accretion rate from the very luminous burst GRB051221 are not astonishing but suggest different values for the f-factors or, alternatively, a NS+BH merger as a source. Newtonian simulations of NS+BH mergers [29, 30, 31, 32, 33, 34, 35] suggest that, for certain mass ratios and EoSs, large torus masses in the range of $0.1 \dots 1 M_{\odot}$ may be formed.

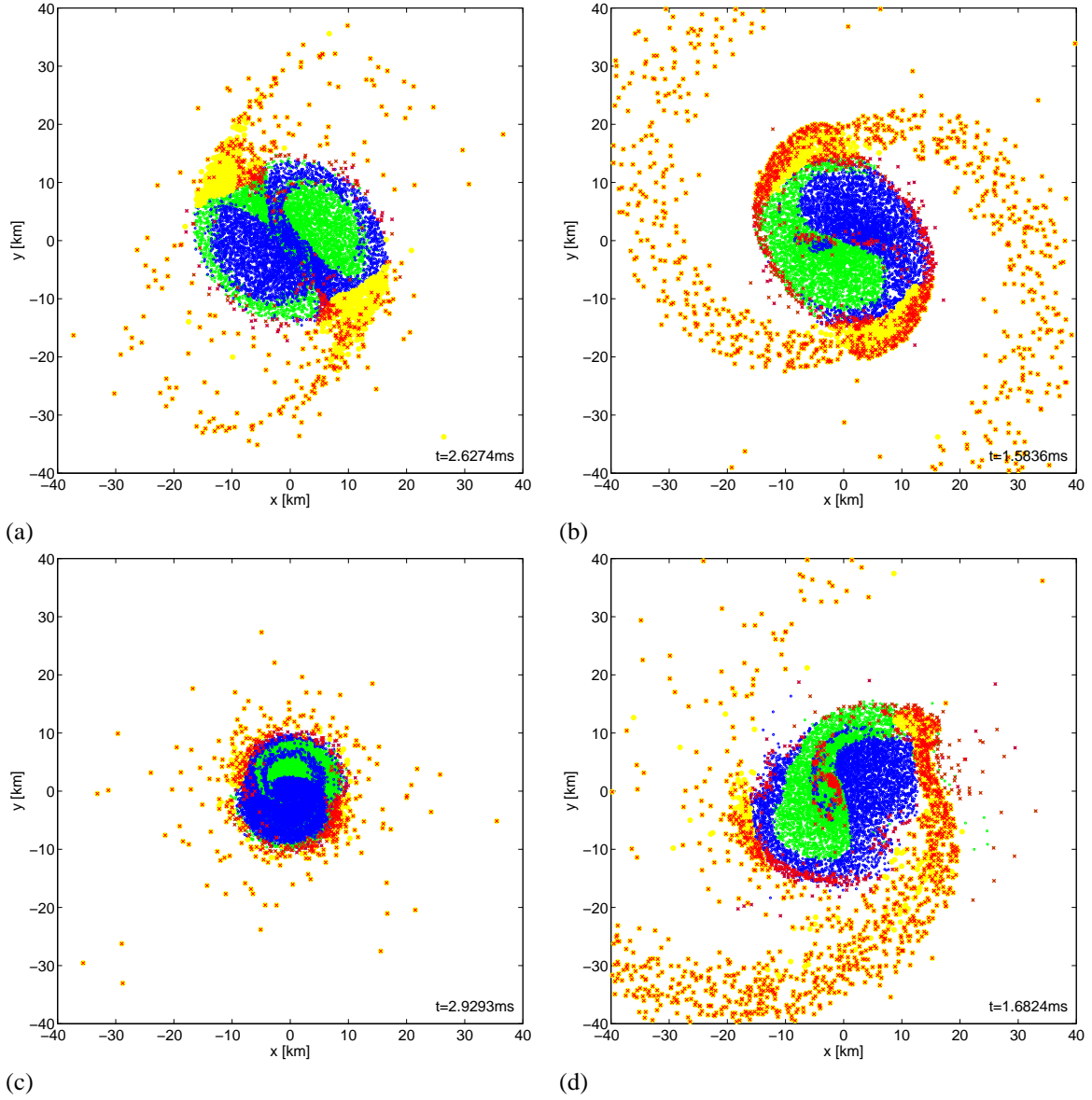


FIGURE 2. Characteristic snapshots of four representative models. Plotted is every 10th SPH particle in a slice around the equatorial plane. The matter of the two NSs is color-coded by green and blue particles. Particles ending up in the torus are plotted in red while the yellow circles represent particles which currently have an angular momentum larger than the angular momentum of the last stable orbit of the merger remnant at the end of the simulation. (By definition, the yellow and red particles coincide at the end of the run.) Panel (a) shows the development of secondary spiral arms in model S1414. Panel (b) shows the large, primary spiral arms in model S1414co. Panel (c) shows the post-merger evolution of model L1414. The merger remnant is much more compact and no secondary spiral arms are forming. As a consequence, the torus is much smaller and is developing on a longer timescale. In panel (d), we see the formation of the large primary spiral arm in model S1216

REFERENCES

1. S. Blinnikov, I. Novikov, T. Perevodchikova, and A. Polnarev, *Soviet. Astron. Letters* **10**, 177 (1984).
2. B. Paczyński, *ApJL* **308**, L43 (1986).
3. D. Eichler, M. Livio, T. Piran, and D. Schramm, *Nature* **340**, 126 (1989).
4. B. Paczyński, *Acta Astron.* **41**, 257 (1991).
5. R. Narayan, B. Paczyński, and T. Piran, *ApJL* **395**, L83 (1992).
6. D. Fox, et al., *Nature* **437**, 845 (2005).

7. J. Hjorth, et al., *ApJ* **630**, L117 (2005).
8. J. Hjorth, et al., *Nature* **437**, 859 (2005).
9. W.-H. Lee, E. Ramirez-Ruiz, and J. Granot, *ApJL* **630**, L165 (2005).
10. J. Bloom, et al., *ApJ* **638**, 354 (2006).
11. S. Woosley, *ApJ* **405**, 273 (1993).
12. M. Ruffert, and H.-T. Janka, *A&A* **344**, 573 (1999).
13. R. Popham, S. Woosley, and C. Fryer, *ApJ* **518**, 356 (1999).
14. S. Rosswog, E. Ramirez-Ruiz, and M. Davies, *MNRAS* **345**, 1077 (2003).
15. W.-H. Lee, E. Ramirez-Ruiz, and D. Page, *ApJ* **632**, 421 (2005).
16. M. A. Aloy, H.-T. Janka, and E. Müller, *A&A* **436**, 273 (2005).
17. R. Oechslin, and T. Janka, *MNRAS*, *in press* (2006).
18. R. Oechslin, T. Janka, and A. Marek, *in preparation* (2006).
19. H. Shen, H. Toki, K. Oyamatsu, and K. Sumiyoshi, *Nucl. Phys. A* **637**, 435 (1998).
20. H. Shen, H. Toki, K. Oyamatsu, and K. Sumiyoshi, *Prog. Theor. Phys.* **100**, 1013 (1998).
21. J. Lattimer, and F. Swesty, *Nucl. Phys.* **A535**, 331 (1991).
22. J. Lattimer, C. Pethik, D. Ravenhall, and D. Lamb, *Nucl. Phys.* **A432**, 646 (1985).
23. A. Levan, et al., *subm. to ApJ Letters*, *astro-ph/0603282* (2006).
24. S. Setiawan, M. Ruffert, and H.-T. Janka, *MNRAS* **352**, 753 (2004).
25. F. Daigne, and R. Mochkovitch, *MNRAS* **296**, 275 (1998).
26. S. Kobayashi, and R. Sari, *ApJ* **551**, 934 (2001).
27. D. Guetta, M. Spada, and E. Waxman, *ApJ* **557**, 399 (2001).
28. W.-H. Lee, and E. Ramirez-Ruiz, *ApJ* **577**, 893 (2002).
29. W. Kluzniak, and W.-H. Lee, *ApJ* **494**, L53 (1998).
30. S. Portegies Zwart, *ApJ* **503**, L53 (1998).
31. W.-H. Lee, and W. Kluzniak, *ApJ* **526**, 178 (1999).
32. H.-T. Janka, T. Eberl, M. Ruffert, and C. Fryer, *ApJ* **527**, L39 (1999).
33. S. Rosswog, R. Speith, and G. Wynn, *MNRAS* **351**, 1121 (2004).
34. S. Rosswog, *ApJ* **634**, 1202 (2005).
35. M. Davies, A. Levan, and A. King, *MNRAS* **356**, 54 (2005).
36. A. Soderberg, et al., *subm. to ApL*, *astro-ph/0601455* (2006).